

Application of the Fractional Fourier Transform to Image Reconstruction in MRI

Vicente Parot,^{1,2} Carlos Sing-Long,^{1,2} Carlos Lizama,^{2,3} Cristian Tejos,^{1,2} Sergio Uribe,^{2,4} and Pablo Irarrazaval^{1,2*}

The classic paradigm for MRI requires a homogeneous B_0 field in combination with linear encoding gradients. Distortions are produced when the B_0 is not homogeneous, and several post-processing techniques have been developed to correct them. Field homogeneity is difficult to achieve, particularly for short-bore magnets and higher B_0 fields. Nonlinear magnetic components can also arise from concomitant fields, particularly in low-field imaging, or intentionally used for nonlinear encoding. In any of these situations, the second-order component is key, because it constitutes the first step to approximate higher-order fields. We propose to use the fractional Fourier transform for analyzing and reconstructing the object's magnetization under the presence of quadratic fields. The fractional Fourier transform provides a precise theoretical framework for this. We show how it can be used for reconstruction and for gaining a better understanding of the quadratic field-induced distortions, including examples of reconstruction for simulated and in vivo data. The obtained images have improved quality compared with standard Fourier reconstructions. The fractional Fourier transform opens a new paradigm for understanding the MR signal generated by an object under a quadratic main field or nonlinear encoding. Magn Reson Med 68:17–29, 2012. © 2011 Wiley Periodicals, Inc. Key words: fractional Fourier transform; magnetic resonance imaging; image reconstruction; field inhomogeneities; off-resonance correction; nonlinear encoding

The standard paradigm for MRI requires a strong magnetic field with uniform intensity and time-varying linear encoding gradients across the entire field of view. However, deviations in the main field are common as uniform fields are physically difficult to achieve and also because of off-resonance effects from susceptibility changes. Such frequency variations introduce an accumulating phase over time, which cannot be demodulated easily as it varies spatially. This problem is worse for stronger fields and for sequences with long acquisition times. Great efforts are put

in building the system with the highest possible homogeneity, for example, with passive or active shimming which partially correct first- and second-order field variations.

Additionally, there has been an increasing interest in spatial encoding by nonhomogeneous, nonbijective spatial encoding magnetic fields (SEMs; Ref. 1). Starting from a general nonlinear field concept, novel techniques including PatLoc (1), O-Space (2), Null Space (3), and Phase-Scrambled imaging (4–6) have all introduced the use of second-order SEMs as the first and simplest approach in simulations, custom-built hardware and experiments (7–12). One of the challenges of these approaches is to have an appropriate reconstruction technique.

Higher-order fields also appear as a natural component of linear gradients. These concomitant fields can be well approximated by quadratic functions (13,14). In several applications, the magnitude of these fields is not negligible and artifacts appear in image reconstructions (15,16), most notably in very low-field or microtesla imaging (17,18).

Several image reconstruction methods have been proposed to correct distortions, or to reconstruct an image produced by nonhomogeneous fields, being an active field of research (19–28). There is a well-known theoretical background for the linear correction approaches, in which an exact analytical solution is provided (19,23). For second-order and arbitrary field maps, there are several correction techniques that typically trade-off correction accuracy for computational load. Some of them are variations of the basic conjugate phase (CP) approach (29–31), which will be relevant to this work.

The fractional Fourier transform (FrFT) is a generalization of the standard Fourier transform (FT) by means of the continuous fractional order a , which covers densely the entire transition between image (or time) domain ($a = 0$) and the Fourier domain ($a = 1$; Ref. 32). The FrFT is a special case of the linear canonical transform and can be defined in several different ways leading to different physical interpretations and thus, it has become useful in many applications (33–35). It has been shown that the FT properties are special cases of FrFT properties (32), and further research has been done in discretization (36,37), fast computation (38), and other aspects of the FrFT related to signal processing (39–42).

It is of general knowledge that the magnetization of an object under a linear magnetic field can be related to the FT of the MR signal due to the mathematical equivalence of the signal with the FT kernel. Similarly, the magnetization of an object under a quadratic field can be related to its FrFT. The kernel of the integral definition of the FrFT presents a resemblance with the MR signal. This fact, along with

¹Department of Electrical Engineering, Pontificia Universidad Católica de Chile, Santiago, Chile.

²Department of Electrical Engineering and Department of Radiology, Pontificia Universidad Católica de Chile, Santiago, Chile.

³Department of Mathematics and Computer Science, Universidad de Santiago de Chile, Santiago, Chile.

⁴Department of Radiology, Pontificia Universidad Católica de Chile, Santiago, Chile.

Grant sponsor: CONICYT; Grant number: Fondecyt 1070674 and 1100529, FONDEF D05110358, and Anillo PBCT-ACT-79.

*Correspondence to: P. Irarrazaval, Ph.D., Department of Electrical Engineering, Pontificia Universidad Católica de Chile, Av. Vicuña Mackenna 4860, Macul 7820436, Santiago, Chile. E-mail: pim@ing.puc.cl

Received 11 January 2011; revised 21 July 2011; accepted 28 July 2011.

DOI 10.1002/mrm.23190

Published online 17 October 2011 in Wiley Online Library (wileyonlinelibrary.com).

the techniques involving second-order SEMs or concomitant fields, places the FrFT as a potentially useful tool due to its inherent connection with the second-order modulation of the MR signal. The Fresnel transform, also a special case of the linear canonical transform, has found a particular use in phase-scrambled imaging. The FrFT provides a wider description of the problem and a stronger formulation through its physical relation to the FT. For the purposes of this work, let a quadratic MR system be one which has a second-order magnetic field as a function of space, with time-varying global amplitude. Thus, systems that have a quadratic main field and/or quadratic SEMs fit into this description.

In this article we present a theoretical description of the relationship between the FrFT and the MR signal in the presence of quadratic fields. This relation provides a theoretical framework to analyze the distortions produced by quadratic fields and allows to define a reconstruction technique. We show how the FrFT corrects substantial phase errors for constant gradient trajectories (two-dimensional discrete Fourier transform (2DFT), for example) and corrects geometric distortions for variable gradients trajectories, such as echo planar imaging (EPI). Furthermore, we also introduce a variable order FrFT, which turns out to be similar to CP with an added weighting function, although its interest is more theoretical than practical as the improvements are minor, and CP is more general, because it is also applicable to arbitrary field deviations.

THEORY

This section explains the connection between the FrFT and quadratic MR systems. This framework allows to analyze the acquired data in a fractional order polar space, from where a visual insight can be extracted.

FrFT

The a -th order FrFT $f_a(\rho) = \mathcal{F}^a\{f\}(\rho)$ of the signal $f(u)$ for $0 < |a| < 2$ can be expressed as an integral transform as (taken from Ref. 32 with a slight change of notation)

$$f_a(\rho) = C_\alpha(\rho) \int f(u) \exp(i\pi[u^2 \cot \alpha - 2\rho u \csc \alpha]) du, \quad [1]$$

$$C_\alpha(\rho) \equiv \exp(i\pi\rho^2 \cot \alpha) \sqrt{1 - i \cot \alpha}, \quad \alpha \equiv a\pi/2, \quad [2]$$

where \cot is the cotangent, and \csc is the cosecant of the argument.

Note that the most notable difference between this equation and the FT is an extra quadratic phase in the kernel.

Throughout this section, u and ρ denote dimensionless variables to maintain formal consistency between the MRI and FrFT contexts. The independent variable ρ is the pseudofrequency in any fractional domain, and u is the particular case of ρ for the 0-th order (the object domain). The relation between the dimensionless u and its dimensional counterpart x will be addressed in the “ ρ - α space” section.

MRI Signal Under a Quadratic Main Field

We will consider the one-dimensional case where the main field is a quadratic function of space and linear encoding

gradients are used. The extension to general quadratic MR systems will be discussed later on. Let $f(u)$ be the magnetization of the object of interest. The MR signal, in a perfect uniform B_0 field, ignoring intrareadout T_1 and T_2 relaxations and after demodulation at the Larmor frequency ω_0 is

$$s(t) = \int f(u) \exp(-i2\pi k(t)u) du, \quad [3]$$

where, as customarily defined, $k(t) = \gamma/2\pi \int_0^t G(\tau) d\tau$ is the k -space trajectory.

Whenever there is an inhomogeneous field $B(u) = B_0 + p(u)$ as a function of space, the magnetization is modulated by a time-dependent phase. For a quadratic field, $p(u) = p_2 u^2 + p_1 u + p_0$. In this case the signal equation becomes

$$s(t) = \exp(-i2\pi p_0 t) \times \int f(u) \exp(i\pi[-2p_2 t u^2 - 2(k(t) + p_1 t)u]) du \quad [4]$$

There is a remarkable similarity between this expression and the FrFT defined in Eq. 1. Consequently, it is natural to think that the FrFT can be used to reconstruct these data.

Link Between the MR Signal and the FrFT

To represent Eq. 4 in the form of Eq. 1, define

$$\alpha(t) = \cot^{-1}(-2p_2 t) \quad \text{and} \quad \rho(t) = \frac{k(t) + p_1 t}{\csc \alpha(t)} = \frac{k(t) + p_1 t}{\sqrt{1 + 4p_2^2 t^2}} \quad [5]$$

In this definition, both α and ρ are functions of time, but it will be omitted for the sake of notation simplicity. Consider $\alpha \in (0, \pi)$, which ensures $\csc \alpha > 0$, and \cot^{-1} invertible, so it can be written $-2p_2 t = \cot \alpha$ and $-2(k(t) + p_1 t) = -2\rho \csc \alpha$. With these variables the signal in Eq. 4 becomes

$$s(t) = \exp(-i2\pi p_0 t) \int f(u) \exp(i\pi[u^2 \cot \alpha - 2\rho u \csc \alpha]) du$$

Using Eq. 1, the signal equation becomes a time-varying order FrFT of the object

$$s(t) = \exp(-i2\pi p_0 t) C_\alpha(\rho)^{-1} f_a(\rho) \quad [6]$$

$$f_a(\rho) = \exp(i2\pi p_0 t) C_\alpha(\rho) s(t).$$

Note that if α were constant and equal to $\pi/2$ (or $a = 1$), the signal equation is recovered in terms of the standard FT. The advantage of this relation is that it provides a well-known framework for working with quadratic terms in the magnetic field.

The two-dimensional (2D) extension is straightforward and is shown in the Appendix.

In a quadratic MR system, both the main field and SEMs can be modeled as quadratic functions of space. In this case, it is clear that the signal of Eq. 3 becomes:

$$s(t) = \exp(-i2\pi p_0 t) \int f(u) \exp(i\pi[h(t)u^2 + g(t)u]) du \quad [7]$$

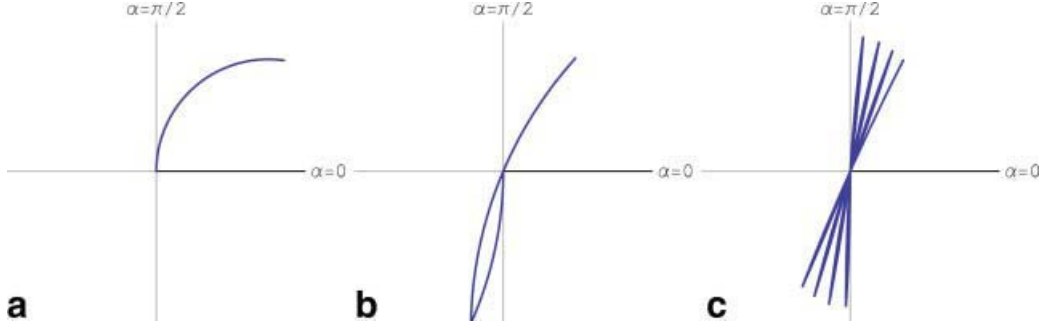


FIG. 1. Examples of typical trajectories over a quadratic field in the polar representation of ρ - α space. **a:** A constant gradient can be represented as a circular path. **b:** A 2DFT bipolar gradient describes two circular arcs. **c:** The polar graph shows the ρ - α space in the readout direction for seven readout echoes of an EPI trajectory. [Color figure can be viewed in the online issue, which is available at wileyonlinelibrary.com.]

for some suitable functions h and g . The change of variables defined in Eq. 5 can be used to deduce α and ρ as functions of t . Therefore, the analysis done for a quadratic main field can be extended to quadratic MR systems with time-varying quadratic fields. However, what follows focuses on the case of a quadratic main field and linear gradients. This allows to perform experiments in a standard MR system, as described in “Materials and Methods” section.

The ρ - α Space

The terms α and ρ in Eq. 5 define a parametric trajectory $(\rho(t), \alpha(t))$ in what we call the ρ - α space. As α is an angle, this space is conveniently represented in polar coordinates. The trajectory in ρ - α space starts immediately after the excitation ($t = 0$) in the frequency or Fourier direction ($\alpha = \pi/2$), and as time passes, it curves toward the object axis ($\alpha = 0$). What follows analyzes some common trajectories using this framework. For the sake of simplicity, the restriction on maximum slew rate is neglected.

Constant Gradient

Let us assume that the readout gradient G_0 is constant and starts at $t = 0$, as would be the case in a projection reconstruction sequence. Assume also that the field is purely quadratic $p(u) = p_2 u^2$. Linear and constant terms can be ignored without loss of generality, because the first is equivalent to a change in the amplitude of the gradient, and the second can be corrected during the signal demodulation. Then $k(t)$ would be $\int_0^t G_0 d\tau = G_0 t$ and the trajectory in ρ - α space would be

$$\alpha(t) = \cot^{-1}(-2p_2 t)$$

$$\rho(t) = \frac{k(t) + p_1 t}{\sqrt{1 + 4p_2^2 t^2}} = \frac{G_0 t}{\sqrt{1 + 4p_2^2 t^2}}$$

which is the parametric form of a circle centered at $(G_0/4p_2, 0)$. Figure 1a shows this trajectory assuming $p_2 < 0$. The trajectory asymptotically approaches the object axis ($\alpha = 0$), as t increases. As expected, for small values of t , the trajectory deviates little from the frequency axis ($\alpha = \pi/2$), and therefore distortions due to field variations are small.

If p_2 tends to zero, the quadratic component of the field vanishes and the center of the circumference located at $G_0/4p_2$ tends to infinity. Equivalently, the ρ - α space trajectory becomes a straight line in the frequency direction

$$\alpha(t) = \cot^{-1}(-2p_2 t) = \frac{\pi}{2}$$

$$\rho(t) = \frac{G_0 t}{\sqrt{1 + 4p_2^2 t^2}} = G_0 t.$$

Standard 2DFT readout

Considering again that the field is $p(u) = p_2 u^2$, now assume that the gradient is formed by a negative pulse of duration t_0 followed by a positive one, as is standard in 2DFT readouts. In this case,

$$k(t) = \int_0^t G(\tau) d\tau = \begin{cases} -G_0 t & 0 < t < t_0 \\ G_0(t - 2t_0) & t_0 < t. \end{cases}$$

Consequently, the trajectory in ρ - α space is given by

$$\alpha(t) = \cot^{-1}(-2p_2 t)$$

$$\rho(t) = \frac{1}{\sqrt{1 + 4p_2^2 t^2}} \times \begin{cases} -G_0 t & 0 < t < t_0 \\ G_0(t - 2t_0) & t_0 < t. \end{cases}$$

This trajectory is formed by two circular arcs. The trajectory describes one arc for the negative gradient centered at $(-G_0/4p_2, 0)$ and continues on the other one centered at $(G_0/4p_2, -G_0 t_0)$, which corresponds to the positive gradient as shown in Fig. 1b.

EPI readout

If the gradient were a train of negative and positive pulses as is used in EPI

$$G(t) = \begin{cases} -G_0 & \text{for } 0 < t < t_0, 3t_0 < t < 5t_0, \dots \\ G_0 & \text{for } t_0 < t < 3t_0, 5t_0 < t < 7t_0, \dots \end{cases}$$

the described ρ - α space trajectory would be composed by a series of circular arcs centered at $(\pm G_0/4p_2, \mp jG_0 t_0/2)$, $j = 0, 1, 2, \dots$ as shown in Fig. 1c.

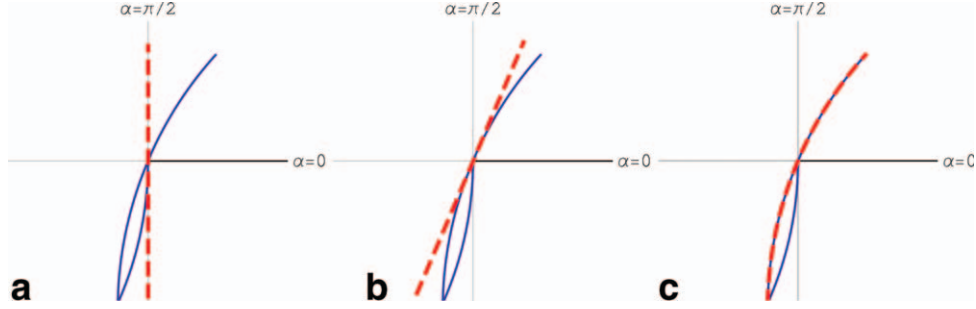


FIG. 2. Example of a one-dimensional 2DFT trajectory in the polar representation of ρ - α space represented by the continuous line and its reconstruction interpretation represented by the dashed line. **a**: Standard Fourier interpretation. **b**: Fractional Fourier interpretation. **c**: Variable order fractional Fourier interpretation.

Spectroscopy

If the sequence has no gradients, as in a pure spectroscopic acquisition, the trajectory will only depend on the linear term of the field p_1

$$\alpha(t) = \cot^{-1}(-2p_2t)$$

$$\rho(t) = \frac{k(t) + p_1t}{\sqrt{1 + 4p_2^2t^2}} = \frac{p_1t}{\sqrt{1 + 4p_2^2t^2}}$$

and will have the shape shown in Fig. 1a, centered at $(p_1/4p_2, 0)$. If $p_1 = 0$, the trajectory is a singularity at the origin of the ρ - α space. In this case, it is more convenient to represent the space in Cartesian coordinates (ρ, a) , and the readout trajectory $\rho = 0$ becomes equivalent to acquiring the continuous component of the FrFT for the orders a .

Reconstruction

In the FrFT framework, the reconstruction problem requires knowing both the pseudofrequency and the transform order where the data was acquired. These can be determined using Eq. 5. The object will be the solution to the inverse of Eq. 6 (ignoring the constant field shift p_0)

$$\hat{f}(u) = \mathcal{F}^{-a}\{f_{\alpha(t)}(\rho(t))\}(u) = \mathcal{F}^{-a}\{C_{\alpha(t)}(\rho(t))s(t)\}(u).$$

This expression explicits the time dependence of α . This dependency implies that the fractional order changes with time and therefore a standard inverse FrFT is not possible. We propose two alternatives for the reconstruction: the inverse FrFT, which assumes an approximation for the ρ - α space; and the variable order inverse fractional Fourier reconstruction (VO-FrFT). These techniques are compared with the standard inverse Fourier reconstruction (FT). Figure 2 shows the actual ρ - α space trajectory and the assumption of the reconstruction scheme for a standard 2DFT readout.

Standard Inverse Fourier Reconstruction

This is equivalent to assuming that $\alpha \equiv \pi/2$, $\cot \alpha \equiv 0$ and $C_{\pi/2}(\rho) \equiv 1$. The reconstructed object is

$$\hat{f}(u) = \mathcal{F}^{-1}\{s(t)\}(u).$$

The samples are acquired in the curved trajectory but are interpreted as being in the frequency axis (vertical dashed line of Fig. 2a). The distortions in the image will depend on how much the trajectory deviates from the vertical line in the ρ - α space. This reconstruction can be computed using the FFT algorithm.

Inverse Fractional Fourier Reconstruction

It assumes that the samples are acquired at a constant order, i.e. on a straight line in ρ - α space during readout, and that locations along the fractional domain are uniformly spaced.

The reconstruction and sampling locations are closer than in the FT reconstruction and the inverse expression is exactly an inverse FrFT

$$\hat{f}(u) = \mathcal{F}^{-\bar{a}}\{C_{\bar{a}}(\rho(t))s(t)\}(u),$$

where \bar{a} (or $\bar{\alpha}$) is the order (or angle for the straight line) at the origin. This reconstruction is a better approximation and improves the accuracy of the reconstructed object's phase over the standard Fourier reconstruction. Using the definitions in Eqs. 1 and 2, it can be seen that

$$\hat{f}(u) = \exp(-i\pi u^2 \cot \bar{\alpha}) |\csc \bar{\alpha}| \int s(t) \exp(i2\pi u \rho \csc \bar{\alpha}) d\rho. \quad [8]$$

In the case of a sequence with multiple echoes during one readout, this approximation may not be useful as the trajectory differs from a single constant line and the origin is sampled with multiple different angles. In the case of an EPI readout (Fig. 1c), the trajectory can be approximated with a constant angle for each echo, which approximates better the angle of each sample. Reconstruction using the inverse FrFT can be implemented using any of the discrete algorithms available in the literature (32), with computation complexity $O(N \log N)$ and additional overhead times when compared with FFT.

Variable Order Inverse Fractional Fourier Reconstruction

This approach uses the actual locations where the data were acquired. To solve the variable order inverse problem we propose a discrete approach, which fits well with the discrete samples and can also provide a continuous

reconstruction. Each sample in ρ - α space (ρ_n, α_n) acquired at $t = t_n$ corresponds to one coefficient of the FrFT of order $a_n = 2\alpha_n/\pi$. Each of these coefficients is the projection of the object into the kernel function of the corresponding fractional order and position. These kernels are commonly known as ‘‘chirp’’ functions and are given by the inverse FrFT of order a_n of a delta function located at $\rho = \rho_n$ (32):

$$\begin{aligned}\Delta_{-a_n}(u) &= \mathcal{F}^{-a_n}\{\delta(\rho - \rho_n)\}(u) \\ &= C_{a_n}^*(\rho_n) \exp(-i\pi[u^2 \cot \alpha_n - 2u\rho_n \csc \alpha_n]),\end{aligned}$$

where $*$ denotes complex conjugate. From the set of all possible chirp functions, the object is projected to the subset of (ρ_n, α_n) pairs corresponding to the sampling locations traversed by the trajectory during readout. Reconstruction from these coefficients is feasible as long as the trajectory is well conditioned. In a discrete sense, this means that the trajectory and sampling locations must define an approximately orthogonal square encoding matrix. From this general idea, whenever a well-conditioned trajectory and uniform sampling density is used, a simple sum of the contributions of each projection can give a good estimation of the generating object. Recalling that the samples are defined by

$$f_{a_n}(\rho_n) = C_{a_n}(\rho_n)s(t_n),$$

this yields an estimation of the object as the weighted sum of all contributions, one for each of N samples,

$$\begin{aligned}\hat{f}(u) &= \sum_{n=1}^N f_{a_n}(\rho_n)\Delta_{-a_n}(u) \\ &= \sum_{n=1}^N |\csc \alpha_n|s(t_n)\exp(-i\pi[u^2 \cot \alpha_n - 2u\rho_n \csc \alpha_n]).\end{aligned}\quad [9]$$

If the uniform sampling density assumption is dropped, it would be necessary to incorporate a factor proportional to $\dot{\rho}(t_n)$ which arises from the underlying discretization of the inverse FrFT integral by Riemann sums. To use this reconstruction method with 2DFT and EPI trajectories, it is assumed that they are approximately well conditioned within a limited quadratic field component, as they are inherently designed for k -space acquisition and not to match ρ - α space positions of orthogonal projections.

The nominal computational complexity of this method is $O(N^2)$, and its implementation cannot be based on the FFT. The 2D extension of this reconstruction method is presented in the Appendix.

The object $\hat{f}(u)$ in Eq. 9 can be evaluated for any continuous value of u . Note that if α_n is substituted by $\pi/2$ this formula becomes the definition of the discrete frequency Fourier transform, or the Discrete Fourier Transform (DFT), if u is also evaluated at discrete values. If α_n is substituted by another fixed angle, other than $\pi/2$, the reconstruction is also the discrete frequency Fourier transform, but with an extra phase and an additional constant scaling factor. This is the discrete version of the inverse FrFT.

It is relevant to note that the CP method reconstructs removing the phase modulation due to field inhomogeneity

from the signal. In one dimension and with uniform sampling density, the CP reconstruction is (29,30)

$$\hat{f}(u) = \sum_{n=1}^N s(t_n)\exp(i2\pi[k_n u + t_n p(u)]), \quad [10]$$

where the pair (t_n, k_n) denotes the sampled trajectory in k -space and $p(u)$ is an arbitrary frequency deviation. Note that this method also assumes the trajectory to be well conditioned, because the independence of the summed functions heavily depends on the trajectory and the arbitrary field $p(u)$. Considering only the first- and second-order terms of its Taylor approximation, the inhomogeneity is reduced to $p(u) = p_2 u^2 + p_1 u$. In this case, the difference between the VO-FrFT and CP can be appreciated in Eq. 9, substituting the definitions in Eq. 5, so that VO-FrFT method can be written as:

$$\hat{f}(u) = \sum_{n=1}^N |\csc \alpha_n|s(t_n)\exp(i2\pi[k_n u + t_n p(u)]).$$

Notably, the VO-FrFT method and a second-order approximated field CP reconstruction differ in the modulating factor $|\csc \alpha_n|$. These weights arise naturally as a consequence of using the FrFT, assuming uniform k -space sampling density. Additionally, this relation shows that the implementation of the VO-FrFT will have a similar computational load as a CP reconstruction method. Consequently, techniques to speed up CP reconstructions can be used for the same purpose for VO-FrFT reconstructions.

Units

So far, ρ and u have been used as dimensionless variables. To ensure the validity of the former analysis and extend it to practical cases, the normalization $u = x/q$ is used, by which

$$f(u) = f(x/q) = \sqrt{q}\tilde{f}(x) \quad [11]$$

with $\tilde{f}(x)$ the dimensional object. The scale parameter q has the same dimension as x . For the purpose of the FrFT implementation, it can be assumed that the magnetization is mostly concentrated within the field of view (FOV), whereas its spectrum is mostly concentrated in the sampled region of k -space. In the time–frequency plane, this means that the energy is mostly concentrated over an elliptic region. The suitable parameter for q is the one that transforms this elliptic region into a circular one. This is achieved by setting $q = FOV/\sqrt{N}$ (43). This normalization is applied independently for each dimension for the n -dimensional case.

MATERIALS AND METHODS

The purpose of the experiments is twofold. First, to study numerically the problem of recovering an image from the MR signal when the main field is quadratic and the gradients are linear. Second, to prove that our reconstruction is useful as a field inhomogeneity correction algorithm for images acquired in traditional systems and when the inhomogeneity has an important quadratic component. All MRI images in this work were acquired

with a Philips Intera 1.5T scanner. Linear shimming was disabled during all acquisitions and no higher-order active shimming was used. The images were acquired using mostly default parameters from preloaded sequences in the system. Complex-valued image reconstructions were performed off-line.

Numerical Phantom

In our first experiment, the MR signal for a 2D, real-valued analytical magnetization phantom was simulated by evaluating Eq. A1 using adaptive quadrature in MATLAB (44), nesting a one-dimensional evaluation for each dimension. The phantom was designed as a simplified version of a real reference phantom with the same dimensions. The acquisition time of each sample and k -space locations were determined considering 2DFT gradients from a standard acquisition. A cartesian matrix of 256×256 samples was simulated with FOV of 25.6×25.6 cm and echo time (TE) = 56 ms. Each complete readout in the sequence takes 28 ms.

Two MR signals were simulated, the first with a uniform B_0 field and the second with a quadratic field with coefficients $p_{2x} = -2.149$ Hz/cm², $p_{2y} = -2.3846$ Hz/cm², $p_{1x} = 0$ Hz/cm, $p_{1y} = 0$ Hz/cm, and $p_0 = 0$ Hz. The quadratic deviation was chosen to be approximately double the measured quadratic component from a real phantom to enhance the effect (while keeping it within a valid physical range). These parameters define the sampling locations of the ρ - α space trajectory, of which fractional domain angles are shown for direction y in Fig. 3 with a solid line. The reconstructed image with standard FT and uniform B_0 was the reference image which incorporates all the inherent distortions of sampling the k -space and the discrete reconstruction. The simulated MR data under a quadratic field was reconstructed with the standard inverse FT, the inverse FrFT, the inverse VO-FrFT, and CP.

To study the performance of these methods when there is error in the estimation of the quadratic component, the reconstruction was repeated using different values of p_{2x} and p_{2y} (from $0 \times$ to $2 \times$ in steps of $0.125 \times$). See the Appendix for a theoretical estimation of uncertainties.

MRI Phantom

In a second experiment, a phantom was scanned with a fast field echo (FFE) EPI sequence, with a scan matrix of 128×128 samples, FOV of 24×24 cm, slice thickness 5 mm, flip angle 23° , and Pulse repetition time/TE = 650/41 ms. These data were acquired with a number of sample averages of 16 using a Q-body coil. The EPI factor in this sequence was 63. Each complete readout in this sequence took 76 ms. These parameters produce a long readout sequence in which there is a noticeable effect of the field inhomogeneities that are inherent to the MR system and object. For the FrFT a constant angle per echo was used. The FrFT approach and the VO-FrFT used a quadratic fit for the measured field map, whereas the CP reconstruction used the measured field map.

In vivo Study

An in vivo study was done scanning the brain of a volunteer, the images were acquired using the same sequence,

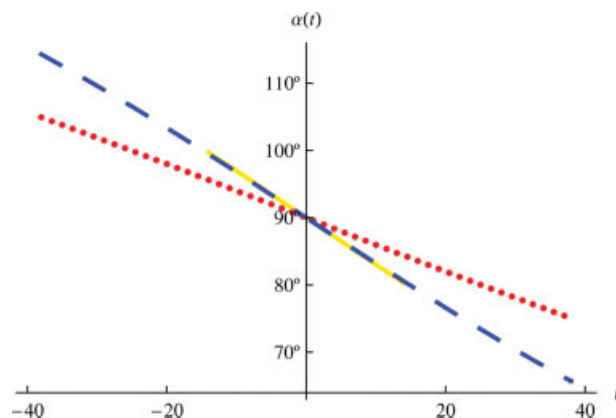


FIG. 3. Fractional angle $\alpha(t)$ throughout the readout of experimental trajectories. The horizontal axis shows time in ms, with echo time in the origin. The solid, dashed, and dotted lines represent the numerical phantom, MRI phantom, and in vivo experiments, respectively. [Color figure can be viewed in the online issue, which is available at wileyonlinelibrary.com.]

except for number of sample average which was now 8 and from the receiving coil which was now a standard quadrature head coil. A slightly angled transversal slice of the brain was selected where the field showed an important quadratic component.

Field Maps

In each experiment, structural images were acquired with short readout time sequences to minimize the effect of field inhomogeneity. The magnetic field was measured from these images with different TE (45).

To fit quadratic functions to the field maps, a maximum likelihood method was used that minimizes the weighted squared error between the measured field map and a parametric separable second-order polynomial. The weights were the mean magnitude of the corresponding pixels. This ensures that the field map information was incorporated correctly depending on the local intensity of the signal and its signal to noise ratio.

In the phantom study, the field map was determined along a structural reference image using $\Delta\text{TE} = 3$ ms and pulse repetition time and TE equal to 14 and 6.1 ms, respectively. A transversal slice of the physical phantom was selected for this study.

For the in vivo study, the anatomy causes further field deviations which cannot be approximated by the fitted function for the entire FOV. An elliptical region of interest was selected.

Image Reconstruction

FT computations were done using FFT and took less than 1 s in all cases. FrFT and VO-FrFT reconstructions were done by computing Eq. A2, which took 10 min for a 256×256 matrix and 1.5 min for a 128×128 matrix, with a Quad-Core 2.4 GHz CPU. The FrFT reconstruction used a constant angle value for each echo, using the value of the angle when $\rho_u = 0$. This is equivalent to compute the 1D inverse FrFT in the readout direction, along which the angles are

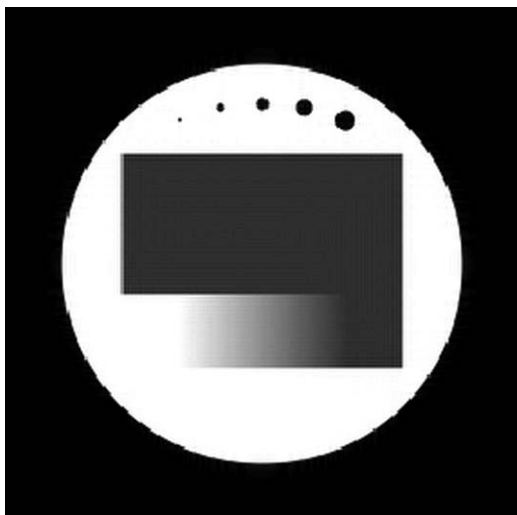


FIG. 4. Reference image for numerical study. This is an inverse Fourier reconstruction of an undistorted simulated signal.

assumed to be constant but not in the phase direction, where the angle is different for each sample. For simplicity of implementation, in this work, we did not take advantage of the fast implementation of the FrFT which would speed it up considerably. The VO-FrFT reconstruction took into account the exact position in ρ - α space of each sample. Distance units of the results were scaled using Eq. 11 to map the estimated object into the dimensional coordinates. CP reconstructions were computed using the 2D extension of Eq. 10, with $p(u)$ the exact measured or simulated frequency deviation and were found to require essentially the same computing time as VO-FrFT reconstructions.

RESULTS

To compare the performance of the reconstruction methods, absolute value images were compared using the root mean squared error (RMSE) and the mean absolute error (MAE). These two metrics heavily penalize images that have only contrast differences, such as an intensity scaling.

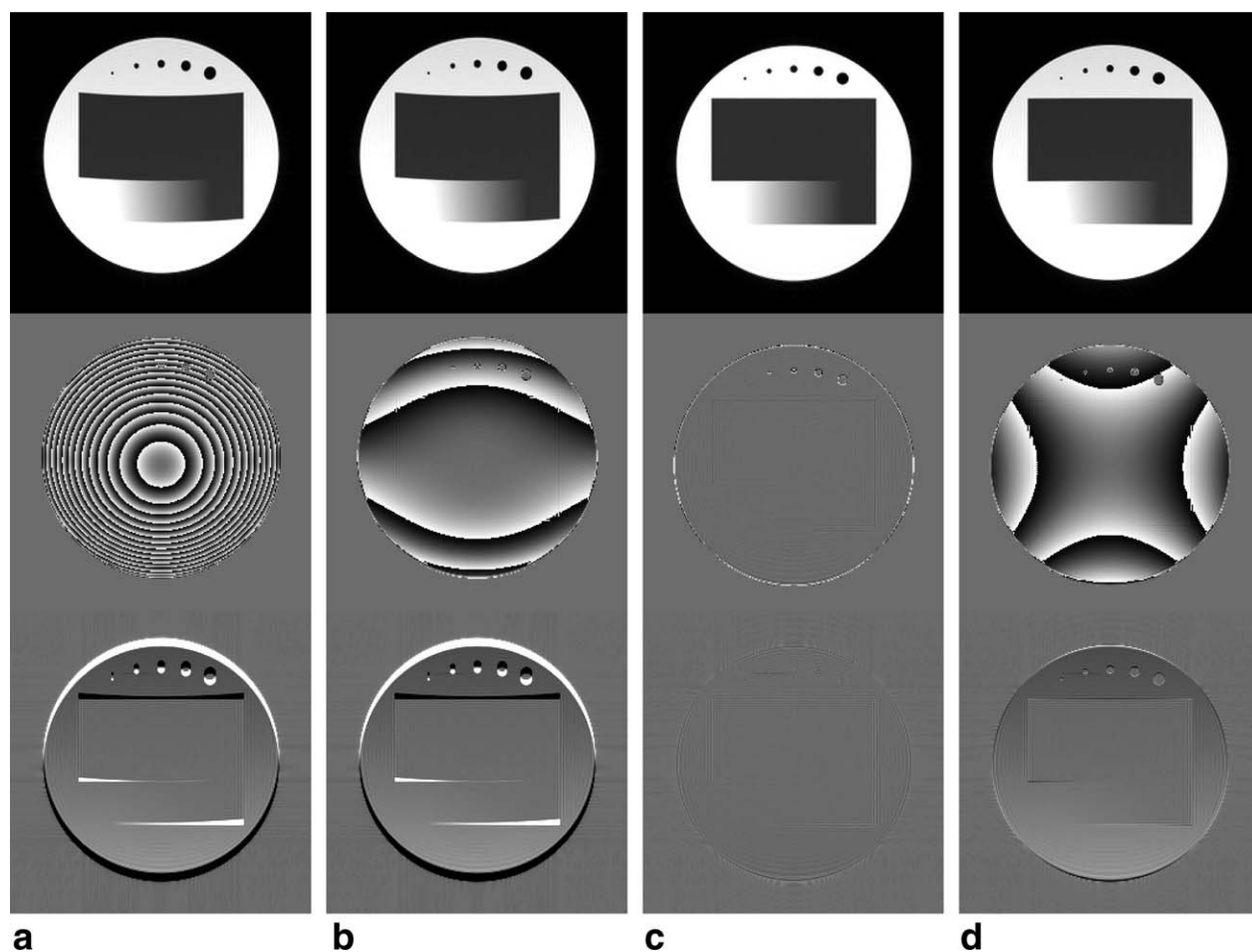


FIG. 5. Reconstruction results for 2DFT simulations with an isotropic quadratic field. In each column, the reconstructed image is shown in magnitude and phase, and it is also shown the difference between absolute images and the reference object. Reconstructed magnitudes range from 0 to 1, and differences are shown with corresponding amplitude from -0.5 to 0.5 . Phase images range from $-\pi$ to π . Phase values have been set to zero, when magnitude is below 5% of the maximum. **a:** Standard inverse Fourier reconstruction. **b:** Inverse fractional Fourier reconstruction. **c:** Variable order inverse fractional Fourier reconstruction considering exact trajectory. **d:** Conjugate phase reconstruction using the simulated field map.

For this reason a third metric was used: mutual information (46), which is invariant to intensity scaling and is needed, because in some cases the reference image was acquired with a different MR contrast than the experimental MR data. Note that, in contrast with the RMSE and the MAE, higher values of mutual information imply that the compared images are closer to each other.

Numerical phantom

The reference image of the numerical phantom can be seen in Fig. 4. The distortions produced by a quadratic field when using the standard Fourier reconstruction can be seen in Fig. 5a. It shows a geometric distortion, characteristic of data acquired under field inhomogeneity, which is proportional to the local field deviation from the central frequency. The phase of the reconstructed image has a complex quadratic modulation, although the analytical phantom did not have phase. An intensity nonuniformity distortion is also noted that can be described as a linear increase of intensity from the lower to the upper region of the phantom. The maximum deviations were within 12% of the correct value. This can be seen also in the intensity difference image (Fig. 5a). As expected, the MR data acquired with a quadratic main field cannot be correctly recovered by the FT method.

As expected from Eq. 8, the FrFT reconstruction shows identical magnitude as the FT reconstruction (Fig. 5a) but with a phase much closer to the actual phase (Fig. 5b). Indeed, the intensity difference image (Fig. 5b) is similar to the one produced by the FT reconstruction. Additionally, both approaches are unable to recover exactly the image geometry. The VO-FrFT reconstruction (Fig. 5c) recovers the original image, without any of the image distortions in magnitude or phase introduced by the FT and FrFT reconstructions. Finally, the CP reconstruction (Fig. 5d) recovers the geometry of the phantom, but it adds a phase that does not belong to the reference image. The intensity of the reconstructed image also shows differences with the reference image, as evidenced by the intensity difference image (Fig. 5d). The visual results are supported by the

Table 1
Comparison of the Reconstruction Error for the Numerical Phantom Study.

Method	RMSE	Mutual information	MAE
FT	20.41	1.33×10^5	7.16
FrFT	20.41	1.33×10^5	7.16
VO-FrFT	1.68	1.58×10^5	0.86
CP	5.35	1.48×10^5	2.82

values for the comparison metrics in Table 1. Only the VO-FrFT reconstructs the exact image, outperforming the CP method. Note that this numerical experiment has been designed as an ideal case to test the reconstruction of the simulated MR signal from a quadratic field and does not necessarily reflect a real setting, where pure quadratic fields are not practically occurring. In many situations, it can also be that the phase is discarded, because only the magnitude image is of interest. Note also that differences in results between the VO-FrFT and CP methods arise in this case solely from the $|\csc \alpha_n|$ weights present in the VO-FrFT computation.

The sensitivity analysis in Fig. 6 shows how the VO-FrFT has the best indexes for all metrics and how these metrics deteriorate as the field used for the reconstruction deviates from the actual field. Note that different metrics discriminate differently both methods. The RMSE shows a very close performance of the VO-FrFT and CP methods (Fig. 6a), being both better than FT and FrFT methods up to a scaling factor of 1.85. Considering mutual information, the VO-FrFT outperforms the other three methods for scale factors as high as 1.9 (Fig. 6b). Considering MAE, the VO-FrFT outperforms all methods for the whole scaling factor range used.

MRI Phantom

The phantom is shown in Fig. 7 (without distortions). The particular combination of our MR system with its intrinsic inhomogeneity and the scanned phantom produced a field

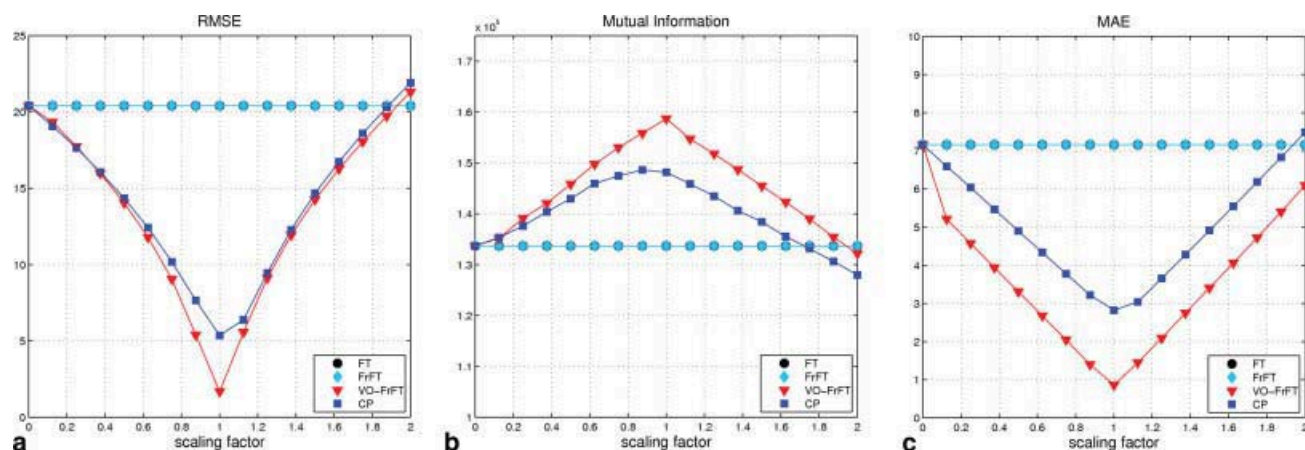


FIG. 6. Measurement of the distortion in absolute reconstructions produced by scaling the quadratic component of the field as an input to the reconstruction method. **a**: Root mean squared error. **b**: Mutual information. **c**: Mean absolute error. [Color figure can be viewed in the online issue, which is available at wileyonlinelibrary.com.]

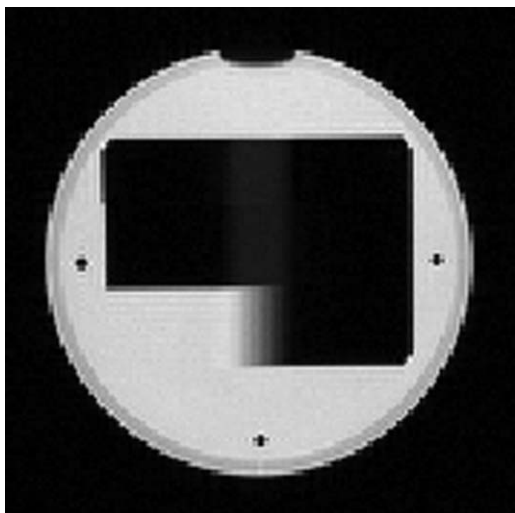


FIG. 7. Low-distortion image used as the reference image for the phantom study.

map that resembles an isotropic quadratic function with its highest intensity in the center of the magnet as shown in Fig. 8. The coefficients of the quadratic function were $p_{2x} = -1.24 \text{ Hz/cm}^2$, $p_{2y} = -1.32 \text{ Hz/cm}^2$, $p_{1x} = -1.81 \text{ Hz/cm}$, $p_{1y} = -1.92 \text{ Hz/cm}$, and $p_0 = 26.29 \text{ Hz}$, and the maximum likelihood fitting error was 2.11 Hz. A profile of the measured field and its fitted function can be seen in Fig. 8c. The

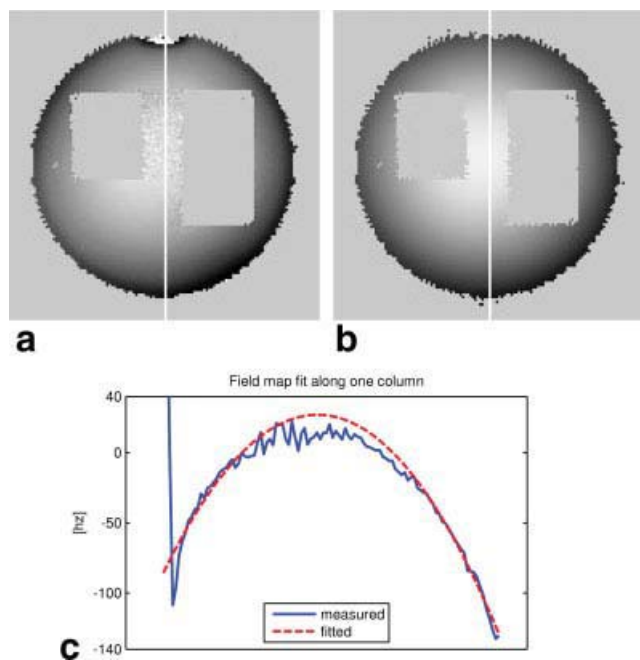


FIG. 8. Field map fit for the MRI phantom study. **a**: Measured field map. **b**: Fitted field map. **c**: Along the marked column, the measured magnetic field (solid line) can be well approximated by a quadratic function (dashed line). Field images range from -140 Hz to 40 Hz . [Color figure can be viewed in the online issue, which is available at wileyonlinelibrary.com.]

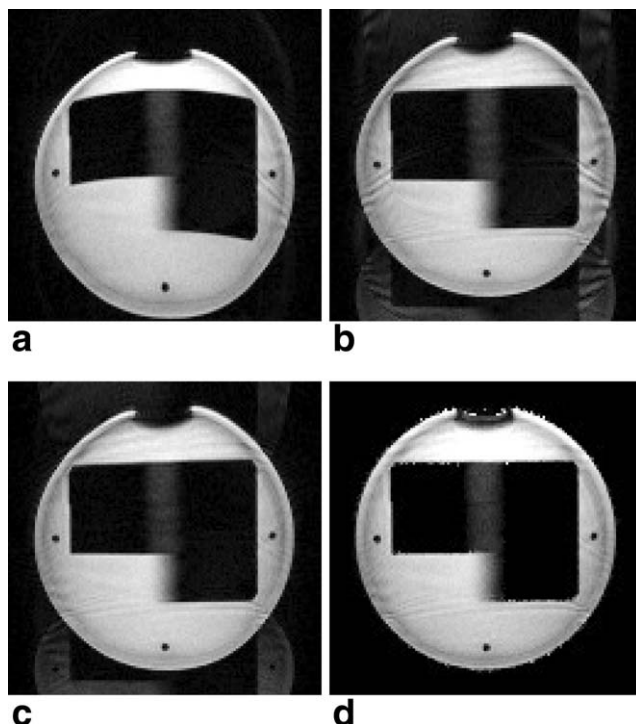


FIG. 9. Reconstruction results for the MRI phantom study. **a**: Standard Fourier reconstruction. **b**: Fractional Fourier reconstruction using the fitted quadratic field map and constant angle approximation in each echo. **c**: Variable order fractional Fourier reconstruction using the fitted quadratic field map. **d**: Conjugate phase reconstruction using the measured field map.

trajectory angles determined by the y -direction coefficients are shown in Fig. 3 with a dashed line.

In this study, the phase information of the object is unknown, because it cannot be acquired with the same contrast as the distorted object without the effect of the quadratic field map. For this reason, only the magnitude of the reconstructions was compared against the magnitude of the low-distortion image.

The FT reconstruction shown in Fig. 9a produces geometric and intensity distortions similar to those observed in the simulation study. The FrFT using constant angle per echoes (Fig. 9b) recovers a better geometry of the sample, albeit with significant Gibbs and ghosting artifacts. Figure 9c shows that the VO-FrFT partially eliminates these artifacts, correctly reconstructing the geometry and intensity of the reference image. We believe that the ghosting artifacts persist, because the field map is not exactly a quadratic function of space. Additionally, some of the artifacts may be related to an incomplete EPI ghosting correction which is present in all reconstructions. Finally, the CP reconstruction (Fig. 9d) also recovers the geometry and corrects the ghosting artifacts but is unable to correct the Gibbs ringing artifacts. The CP reconstruction additionally shows distortions related to noise that are present only in this approach. After CP, the VO-FrFT method has the best reconstruction, as can be seen in Table 2. The difference between VO-FrFT and CP can be explained by a trade-off between the ghosting artifacts in the VO-FrFT reconstruction versus the noise present in the CP reconstruction.

Table 2
Comparison of the Reconstruction Error for the MRI Phantom Study

Method	RMSE	Mutual information	MAE
FT	60.64	1.42×10^5	31.07
FrFT	99.89	1.19×10^5	65.31
FrFT (c.p.e)	35.08	1.51×10^5	21.28
VO-FrFT	33.63	1.51×10^5	19.61
CP	28.03	1.59×10^5	15.73

In vivo Study

Figure 10 shows the low-distortion image for the volunteer experiment. The field can be approximated by a quadratic function within an elliptical region of interest as shown in Fig. 11. The coefficients for the fitted quadratic function were $p_{2x} = -0.23 \text{ Hz/cm}^2$, $p_{2y} = -0.78 \text{ Hz/cm}^2$, $p_{1x} = 0.11 \text{ Hz/cm}$, $p_{1y} = 5.28 \text{ Hz/cm}$ and $p_0 = 62.08 \text{ Hz}$, and the maximum likelihood fitting error was 0.09 Hz. The trajectory angles determined by the y -direction coefficients are plotted in Fig. 3 with a dotted line. Figure 10 also shows a superimposed contour showing some key geometric features of the sample, as a visual aid for comparing the geometric distortions in the reconstructions. The FT reconstruction (Fig. 12a) presents geometric distortions in agreement with the artifacts observed in the numerical and phantom experiments. The FrFT reconstruction with

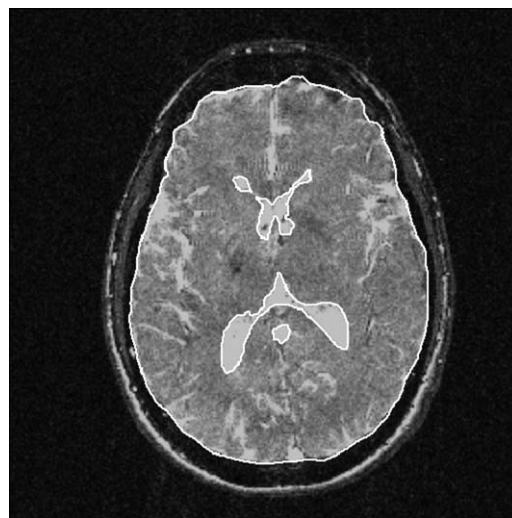


FIG. 10. Low-distortion image used as the reference image for the in vivo study. The superimposed contours show the location of some key features in the image.

constant angle in each echo (Fig. 12b) corrects most of the geometric distortions present in the FT reconstruction (Fig. 12c), especially in the region of interest, where the fitted quadratic function is a close approximation of the field

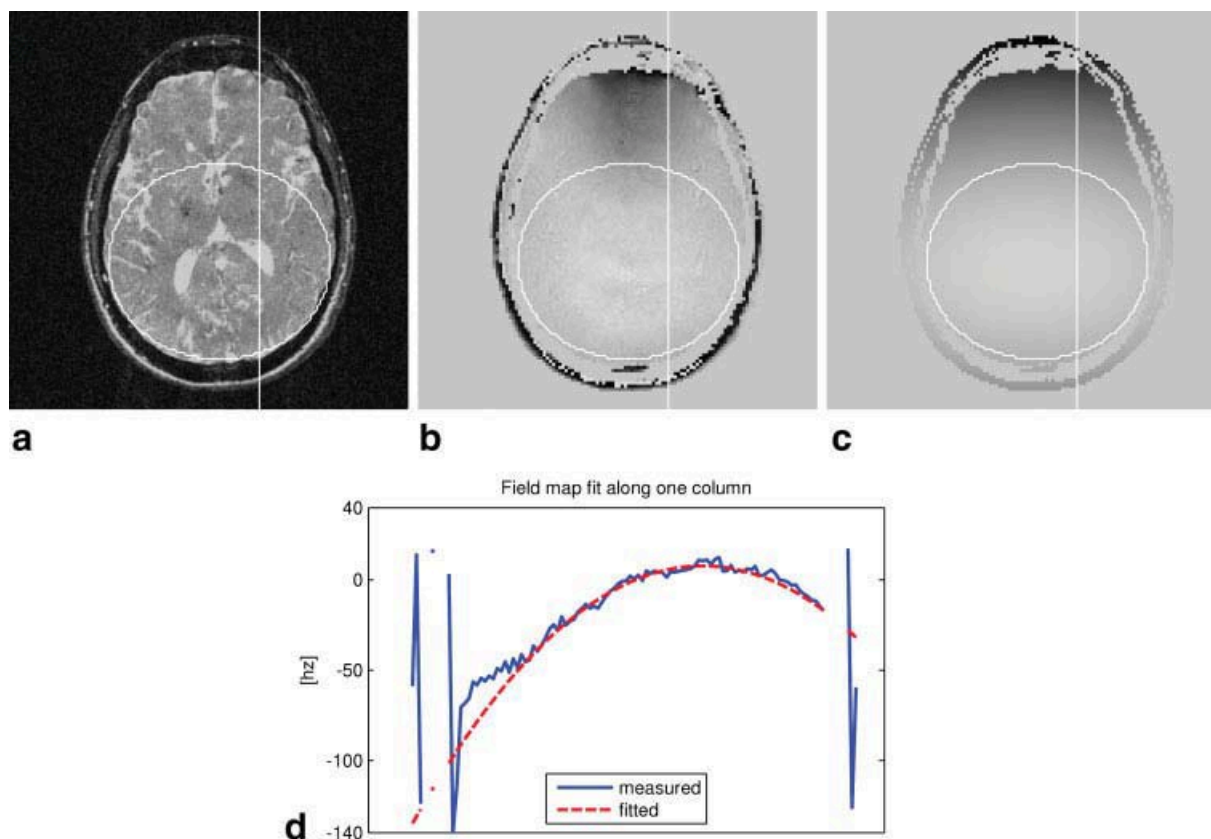


FIG. 11. Field map for the in vivo study. **b**: Measured field map. **c**: Fitted field map. Within the elliptical region of interest in **(a)**, the measured magnetic field can be approximated by a quadratic function as shown in **(d)** with solid and dashed lines, respectively, for the marked column. Field images range from -140 Hz to 40 Hz . [Color figure can be viewed in the online issue, which is available at wileyonlinelibrary.com.]

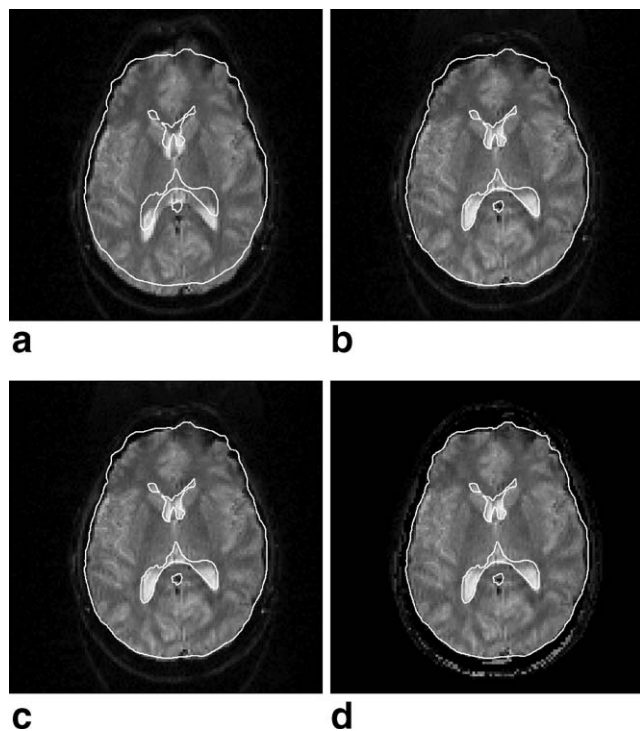


FIG. 12. Reconstruction results for in vivo study. The superimposed contours show the location of some key features of the reference image in Fig. 10. **a**: Standard Fourier reconstruction. **b**: Fractional Fourier reconstruction using the fitted quadratic field map and constant angle approximation in each echo. **c**: Variable order fractional Fourier reconstruction using the fitted quadratic field map. **d**: Conjugate phase reconstruction using the measured field map.

map. The VO-FrFT reconstruction is very similar to the FrFT reconstruction, as the constant angle in each echo is a close approximation of the exact angles of the trajectory in each sample. Finally, the CP reconstruction (Fig. 12d) shows both geometric and intensity artifacts, along with the noise artifacts present in Fig. 9d. In this case, the quantitative comparison depends on which metric is used, as can be seen in Table 3. For example, the MAE shows that the FrFT with constant angle per echo and VO-FrFT are those with the least reconstruction errors, whereas the RMSE and mutual information show that the CP reconstruction is the one with the least reconstruction errors.

DISCUSSION AND CONCLUSIONS

Traditionally, MRI reconstruction is done by an inverse FT. This method rests on the base that the object has been magnetized with a perfectly uniform magnetic field and encoded using linear gradients. In a situation where these conditions do not hold and nonlinear fields come into account, second-order components are their first and simplest approximation.

We presented a new framework for quadratic field MR analysis based on the FrFT. It establishes the theoretical relation between image space and quadratic magnetic field signal frequency space, allowing native second-order field image reconstruction (or correction). The FrFT transform, which is a generalization of the FT, has a quadratic phase

term in its integral kernel, so that there is a natural link between the signal obtained from an object magnetized with a quadratic field and its FrFT. This new framework and the newly introduced ρ - α space give a visual insight to the MR acquisition process and also provide a meaningful graphical representation that shows the relation between the image domain, the standard k -space and FrFT domains. The theoretical derivation is based on the presence of a quadratic static main field and linear encoding gradients and can be extended to a general quadratic system where the quadratic field can be a combination of main field and time-varying encoding gradients.

The FrFT reconstruction with a fixed order for the entire readout corrects phase, and a fixed order for each echo in a multiple echo trajectory corrects geometric distortions, as compared to the traditional FT. From a practical point of view, this is an important improvement when the reconstruction time is important, because the FrFT can be computed with a fast algorithm. Additional work is needed to explore possible combinations of FrFT geometric correction with deformation techniques such as the gradwarp algorithm (47) that would enable to map a geometrically distorted but otherwise artifact-free image from FT reconstruction to the corrected geometry of the FrFT reconstruction.

Numerical experiments showed that the VO-FrFT, can effectively reconstruct MR signals under simulated quadratic fields, correcting geometry and intensity distortions better than FT and CP reconstructions. Experiments in an actual MR system show that, under nearly quadratic fields, our method is able to approximately reconstruct the image and correct some of its geometric distortions, improving over the FT reconstruction, but not exceeding the CP correction, which takes into account not only second-order components but also the exact measured field. The VO-FrFT method should not be preferred over the CP method for inhomogeneity correction, unless the non-homogeneous field component is exactly a second-order function.

One effect of analyzing the MR data using ρ - α space is that it is scaled down by a factor $\csc \alpha_n \geq 1$. This scaling is not homogeneous in k -space but depends on the time map of the sequence. For a given sequence planned for ordinary k -space acquisition, this fact is manifested as a resolution loss. These resolution losses could be reduced using stronger gradients with an ordinary sequence or modifying the sequence to fill ρ - α space at corrected locations. Additionally, new trajectories should be designed to fill ρ - α space in order to meet image resolution requirements. Theoretical advances are also needed to replace the Nyquist sampling rate for k -space with a similar criterion which

Table 3
Comparison of the Reconstruction Error for the In vivo Study

Method	RMSE	Mutual information	MAE
FT	14.02	1.28×10^5	6.81
FrFT	13.06	1.34×10^5	6.09
FrFT (c.p.e)	13.00	1.33×10^5	5.84
VO-FrFT	13.00	1.33×10^5	5.84
CP	12.59	1.39×10^5	6.31

would indicate how information density is distributed along ρ - α space.

Our approach based on the FrFT gives a new theoretical MR framework between image space and signal space for quadratic field MR systems, allowing native image reconstruction for second-order main fields.

APPENDIX A: EXTENSION TO TWO DIMENSIONS

To extend the correspondence between the signal equation and the FrFT definition derived in ‘‘Link Between the MR signal and the FrFT’’ section, it can be written in vector form using the separable FrFT definition. In two dimensions, the FrFT is (32)

$$f_{\mathbf{a}}(\boldsymbol{\rho}) = C_{\alpha}(\boldsymbol{\rho}) \int f(\mathbf{u}) \exp(i\pi(\mathbf{u}^T \mathbf{A} \mathbf{u} - 2\mathbf{u}^T \mathbf{B} \boldsymbol{\rho})) d\mathbf{u}$$

with

$$\mathbf{u} = \begin{bmatrix} u \\ v \end{bmatrix}, \quad \boldsymbol{\rho} = \begin{bmatrix} \rho_u \\ \rho_v \end{bmatrix}, \quad \mathbf{a} = \begin{bmatrix} a_u \\ a_v \end{bmatrix}, \quad \boldsymbol{\alpha} = \mathbf{a} \frac{\pi}{2} = \begin{bmatrix} \alpha_u \\ \alpha_v \end{bmatrix}$$

$$\mathbf{A} = \begin{bmatrix} \cot \alpha_u & 0 \\ 0 & \cot \alpha_v \end{bmatrix}, \quad \mathbf{B} = \begin{bmatrix} \csc \alpha_u & 0 \\ 0 & \csc \alpha_v \end{bmatrix}$$

and $C_{\alpha}(\boldsymbol{\rho}) = \sqrt{1 - i \cot \alpha_u} \sqrt{1 - i \cot \alpha_v} \exp(i\pi \boldsymbol{\rho}^T \mathbf{A} \boldsymbol{\rho})$.

To write the signal equation in 2D, the field can be written as $p(\mathbf{u}) = \mathbf{u}^T \mathbf{p}_2 \mathbf{u} + \mathbf{u}^T \mathbf{p}_1 + p_0$, with

$$\mathbf{p}_1 = \begin{bmatrix} p_{1u} \\ p_{1v} \end{bmatrix} \text{ and } \mathbf{p}_2 = \begin{bmatrix} p_{2u} & 0 \\ 0 & p_{2v} \end{bmatrix},$$

so that it becomes

$$s(t) = \exp(-i2\pi p_0 t) \times \int f(\mathbf{u}) \exp(i\pi(-2\mathbf{u}^T \mathbf{p}_2 \mathbf{u} t - 2\mathbf{u}^T (\mathbf{k}(t) + \mathbf{p}_1 t))) d\mathbf{u} \quad [\text{A1}]$$

with $\mathbf{k}(t) = [k_u(t) \ k_v(t)]^T$, expanded as

$$s(t) = \exp(-i2\pi p_0 t) \iint f(u, v) \exp(-i2\pi((p_{2u} u^2 + p_{2v} v^2) t + (k_u(t) + p_{1u} t)u + (k_v(t) + p_{1v} t)v)) dudv.$$

Note that it is also assumed that the second-order term of the field is diagonal in the coordinate axis, i.e. the terms outside the diagonal of \mathbf{p}_2 are zero to match the separable form of the FrFT. If this is not the case, a change of variables can be performed on x, y , and u, v to diagonalize this term. Note that both \mathbf{A} and \mathbf{B} are diagonal matrices that depend on $\boldsymbol{\alpha}$. A four-dimensional ρ - α space is defined by the change of variables

$$\begin{aligned} \cot \alpha_u &= -2p_{2u} t \\ \cot \alpha_v &= -2p_{2v} t \\ \rho_u \csc \alpha_u &= k_u(t) + p_{1u} t \\ \rho_v \csc \alpha_v &= k_v(t) + p_{1v} t \end{aligned}$$

which is equivalent to solve for $\boldsymbol{\alpha}$ and $\boldsymbol{\rho}$ the matrix equations $\mathbf{A}(\boldsymbol{\alpha}) = -2\mathbf{p}_2 t$ and $\mathbf{B}(\boldsymbol{\alpha})\boldsymbol{\rho} = \mathbf{k}(t) + \mathbf{p}_1 t$. Finally, the

signal equation is expressed in terms of a 2D varying-order FrFT as

$$s(t) = \exp(-i2\pi p_0 t) C_{\alpha}(\boldsymbol{\rho})^{-1} f_{\mathbf{a}}(\boldsymbol{\rho})$$

Similarly, the 2D extension of the reconstruction method presented in Eq. 9 is

$$\hat{f}(\mathbf{u}) = \sum_{n=1}^N |\det(\mathbf{B}_n)| s(t_n) \exp(-i\pi[\mathbf{u}^T \mathbf{A}_n \mathbf{u} - 2\mathbf{u}^T \mathbf{B}_n \boldsymbol{\rho}_n]) \quad [\text{A2}]$$

or, expanding the matrix terms,

$$\begin{aligned} \hat{f}(u, v) &= \sum_{n=1}^N |\csc \alpha_{un} \csc \alpha_{vn}| s(t_n) \exp(-i\pi[\cot \alpha_{un} u^2 \\ &+ \cot \alpha_{vn} v^2 - 2\rho_{un} \csc \alpha_{un} u - 2\rho_{vn} \csc \alpha_{vn} v]). \end{aligned}$$

APPENDIX B: SAMPLING ERRORS

In practice, there is a degree of uncertainty on the estimated values t_n and k_n for the ρ - α space. In the following analysis, differences between the real and estimated values are denoted as δt_n and δk_n respectively. Additionally, the estimation of the values for p_2 , p_1 , and p_0 will also introduce a degree of uncertainty. The difference between the real and estimated value is denoted as δp_2 , δp_1 , and δp_0 , respectively. To perform an accurate analysis and reconstruction using the proposed method, it is important to determine the impact of these uncertainties on the computed values ρ_n and α_n . From Eq. 5, the uncertainty $\delta \alpha_n$ on α_n will be, to first order

$$\delta \alpha_n = \frac{2p_2}{1 + 4p_2^2 t_n^2} \delta t_n + \frac{2t_n}{1 + 4p_2^2 t_n^2} \delta p_2$$

The first term decreases quadratically in time, with values proportional to the errors in measuring t_n , whereas the second term decreases linearly in time, and achieves a maximum value $\delta p_2 / 2p_2$, i.e., one-half of the relative error in measuring p_2 . The uncertainty $\delta \rho_n$ in measuring ρ_n will be, to first order

$$\begin{aligned} \delta \rho_n &= \sin \alpha_n \delta k_n + t_n \sin \alpha_n \delta p_1 \\ &- 4 \frac{p_2 t_n (k_n + p_1 t_n) (p_2 \delta t_n + t_n \delta p_2)}{(1 + 4p_2^2 t_n^2)^{3/2}} \end{aligned}$$

It is clear that the first term remains bounded and proportional to the error in measuring k_n . The second term produces an error that increases in time proportionally to the uncertainty in measuring p_1 . Finally, the third term behaves as $O(k_n t_n^{-2})$ with respect to δt_n , $O(t_n^{-1})$ with respect to δt_n and $O(1)$ with respect to δp_2 .

REFERENCES

- Hennig J, Welz A, Schultz G, Korvink J, Liu Z, Speck O, Zaitsev M. Parallel imaging in non-bijective, curvilinear magnetic field gradients: a concept study. *Magn Reson Mater Phys, Biol Med* 2008;21:5–14.
- Stockmann J, Ciris P, Galiana G, Tam L, Constable R. O-space imaging: highly efficient parallel imaging using second-order nonlinear fields as encoding gradients with no phase encoding. *Magn Reson Med* 2010;64:447–456.

3. Tam L, Stockmann JP, Constable RT. Null Space Imaging: a Novel Gradient Encoding Strategy for Highly Efficient Parallel Imaging. In: Proc. Joint Annual Meeting ISMRM-ESMRMB, 2010; p. 2868.
4. Wedeen V, Chao Y, Ackerman J. Dynamic range compression in MRI by means of a nonlinear gradient pulse. *Magn Reson Med* 1988;6: 287–295.
5. Ito S, Yamada Y. Alias-free image reconstruction using Fresnel transform in the phase-scrambling Fourier imaging technique. *Magn Reson Med* 2008;60:422–430.
6. Zaitsev M, Schultz G, Hennig J. Extended Anti-Aliasing Reconstruction for Phase-Scrambled MRI with Quadratic Phase Modulation. In: Proc. ISMRM, 2009; p. 2859.
7. Schultz G, Weber H, Gallichan D, Hennig J, Zaitsev M. Image reconstruction from radially acquired data using multipolar encoding fields. In: Proc. Joint Annual Meeting ISMRM-ESMRMB, 2010; p. 82.
8. Haas M, Ullmann P, Schneider JT, Ruhm W, Hennig J, Zaitsev M. Large tip angle parallel excitation using nonlinear non-bijective patloc encoding fields. In: Proc. Joint Annual Meeting ISMRM-ESMRMB, 2010; p. 4929.
9. Lin FH, Vesanen P, Witzel T, Ilmoniemi R, Hennig J. Parallel Imaging Technique Using Localized Gradients (Patloc) Reconstruction Using Compressed Sensing (cs). In: Proc. Joint Annual Meeting ISMRM-ESMRMB, 2010; p. 546.
10. Cocosco CA, Dewdney AJ, Dietz P, Semmler M, Welz AM, Gallichan D, Weber H, Schultz G, Hennig J, Zaitsev M. Safety Considerations for a Patloc Gradient Insert Coil for Human Head Imaging. In: Proc. Joint Annual Meeting ISMRM-ESMRMB, 2010; p. 3946.
11. Welz AM, Gallichan D, Cocosco C, Kumar R, Jia F, Snyder J, Dewdney A, Korvink J, Hennig J, Zaitsev M. Characterisation of a Patloc Gradient Coil. In: Proc. Joint Annual Meeting ISMRM-ESMRMB, 2010; p. 1527.
12. Stockmann JP, Constable RT. An assessment of o-space imaging robustness to local field inhomogeneities. In: Proc. Joint Annual Meeting ISMRM-ESMRMB, 2010; p. 549.
13. Bernstein MA, Zhou XJ, Polzin JA, King KF, Ganin A, Pelc NJ, Glover GH. Concomitant gradient terms in phase contrast MR: analysis and correction. *Magn Reson Med* 1998;39:300–308.
14. King KF, Ganin A, Zhou XJ, Bernstein MA. Concomitant gradient field effects in spiral scans. *Magn Reson Med* 1999;41:103–112.
15. Sica CT, Meyer CH. Concomitant gradient field effects in balanced steady-state free precession. *Magn Reson Med* 2007;57:721–730.
16. Du YP, Zhou XJ, Bernstein MA. Correction of concomitant magnetic field-induced image artifacts in nonaxial echo-planar imaging. *Magn Reson Med* 2002;48:509–515.
17. Yablonskiy DA, Sukstanskii AL, Ackerman JJ. Image artifacts in very low magnetic field MRI: the role of concomitant gradients. *J Magn Reson* 2005;174:279–286.
18. Myers WR, Mossle M, Clarke J. Correction of concomitant gradient artifacts in experimental microtesla MRI. *J Magn Reson* 2005;177:274–284.
19. Akel JA, Rosenblitt M, Irarrazabal P. Off-resonance correction using an estimated linear time map. *Magnetic Resonance Imaging* 2002;20:189–198.
20. Chen W, Meyer CH. Semiautomatic off-resonance correction in spiral imaging. *Magn Reson Med* 2008;59:1212–1219.
21. Chen W, Sica CT, Meyer CH. Fast conjugate phase image reconstruction based on a chebyshev approximation to correct for b0 field inhomogeneity and concomitant gradients. *Magn Reson Med* 2008;60:1104–1111.
22. Fessler JA, Lee S, Olafsson VT, Shi HR, Noll DC. Toeplitz-based iterative image reconstruction for MRI with correction for magnetic field inhomogeneity. *IEEE Trans Signal Process* 2005;53:3393–3402.
23. Irarrazabal P, Meyer CH, Nishimura DG, Macovski A. Inhomogeneity correction using an estimated linear field map. *Magn Reson Med* 1996;35:278–282.
24. Manjón JV, Lull JJ, Carbonell-Caballero J, García-Martí G, Martí-Bonmatí L, Robles M. A nonparametric MRI inhomogeneity correction method. *Med Image Anal* 2007;11:336–345.
25. Noll DC, Fessler JA, Sutton BP. Conjugate phase MRI reconstruction with spatially variant sample density correction. *IEEE Trans Med Imaging* 2005; 24:325–336.
26. Sutton BP, Noll DC, Fessler JA. Fast, iterative image reconstruction for MRI in the presence of field inhomogeneities. *IEEE Trans Med Imaging* 2003;22:178–188.
27. Vovk U, Pernus F, Likar B. MRI intensity inhomogeneity correction by combining intensity and spatial information. *Phys Med Biol* 2004;49:4119–4133.
28. Lee JY, Greengard L. The type 3 nonuniform FFT and its applications. *J Comput Phys* 2005;206:1–5.
29. Maeda A, Sano K, Yokoyama T. Reconstruction by weighted correlation for MRI with time-varying gradients. *IEEE Trans Med Imaging* 1988;7:26–31.
30. Noll DC, Meyer CH, Pauly JM, Nishimura DG, Macovski A. A homogeneity correction method for magnetic resonance imaging with time-varying gradients. *IEEE Trans Med Imaging* 1991;10:629–637.
31. Schomberg H. Off-resonance correction of MR images. *IEEE Trans Med Imaging* 1999;18:481–495.
32. Ozaktas HM, Kutay MA, Zalevsky Z. The fractional Fourier transform with applications in optics and signal processing. Chichester, NY: Wiley, 2001.
33. Ozaktas HM, Mendlovic D. Fourier transforms of fractional order and their optical interpretation. *Opt Commun* 1993;101:163–169.
34. Ozaktas HM, Mendlovic D. Fractional Fourier optics. *J Opt Soc Am A* 1995;12:743–751.
35. Yetik IS. Image representation and compression with the fractional Fourier transform. *Opt Commun* 2001;197:275–278.
36. Candan C, Kutay MA, Ozaktas HM. The discrete fractional Fourier transform. *IEEE Trans Signal Process* 2000;48:1329–1337.
37. Ozaktas HM, Sumbul U. Interpolating between periodicity and discreteness through the fractional Fourier transform. *IEEE Trans Signal Process* 2006;54:4233–4243.
38. Bultheel A. Computation of the fractional Fourier transform. *Appl Comput Harmonic Anal* 2004;16:182–202.
39. Guven HE, Ozaktas HM, Cetin AE, Barshan B. Signal recovery from partial fractional Fourier domain information and its applications. *IET Signal Process* 2008;2:15–25.
40. Ozaktas HM, Barshan B, Mendlovic D, Onural L. Convolution, filtering, and multiplexing in fractional Fourier domains and their relation to chirp and wavelet transforms. *J Opt Soc Am* 1994;11:547–559.
41. Ozaktas HM, Arikan O, Kutay MA, Bozdogat G. Digital computation of the fractional Fourier transform. *IEEE Trans Signal Process* 1996;44:2141–2150.
42. Ozaktas HM, Barshan B, Mendlovic D. Convolution and filtering in fractional Fourier domains. *Opt Rev* 1994;1:15–16.
43. Koc A, Ozaktas HM, Candan C, Kutay MA. Digital computation of linear canonical transforms. *IEEE Trans Signal Process* 2008;56:2383–2394.
44. Shampine LF. Vectorized adaptive quadrature in matlab. *J Comput Appl Math* 2008;211:131–140.
45. Schneider E, Glover G. Rapid in vivo proton shimming. *Magn Reson Med* 1991;18:335–347.
46. Pluim J, Maintz J, Viergever M. Mutual information based registration of medical images: a survey. *IEEE Trans Med Imaging* 2003;22:986–1004.
47. Glover GH, Pelc NJ (inventors). Method for correcting image distortion due to gradient nonuniformity. US patent 4,591,789. December 23, 1983. Assignee: General Electric Company.